ADVANCED ELECTRONIC MATERIALS Open Access
www.advelectronicmat.de

GeSn-on-Si Avalanche Photodiodes with High Responsivity and Low Dark Current

Maurice Wanitzek, Harishnarayan Ramachandra, Christian Spieth, Alwin Daus, Jörg Schulze, and Michael Oehme*

GeSn-on-Si avalanche photodiodes (APDs) are emerging as a promising solution for low-light detection in the short-wave infrared (SWIR) spectral range, including applications in imaging and telecommunications. In this work, key challenges such as high dark current and limited responsivity are addressed by demonstrating devices, which combine low noise with high signal amplification, while remaining compatible with silicon-based technology. GeSn-on-Si APDs with various Sn concentrations up to 1.9% are fabricated and characterized. The GeSn layers are grown pseudomorphically on Ge virtual substrates on Si wafers using molecular beam epitaxy. The devices comprise a double-mesa structure and exhibit a dark current dominated by a perimeter leakage path, independent of the Sn content. A dark current below 1 µA is maintained up to the onset of avalanche breakdown, marking a significant improvement compared to prior work. A record-high responsivity of 14.7 A W^{-1} is achieved at 1550 nm for the APD with 1.9% Sn. Through impulse response measurements, the 3-dB bandwidth is determined to 1.2 GHz on devices with an 80 µm diameter, resulting in a responsivity-bandwidth-product of 17.6 A W^{-1} GHz^{-1}. These results highlight the potential of GeSn-on-Si APDs for high-performance, low-light applications in the SWIR range.

1. Introduction

Avalanche photodiodes (APDs) are widely used in applications requiring high responsivity, including optical communication, light detection and ranging (LiDAR), and imaging in the short-wave infrared (SWIR) region.[1–3] With applications spanning from quantum information systems to environmental monitoring, detection in the SWIR spectral range (1.1–3 µm) has become increasingly critical due to its unique advantages: it offers superior atmospheric transmission, reduced solar background, and eye-safe operation at wavelengths around 1550 nm.[4] SWIR imaging has proven indispensable in fields like remote sensing, medical diagnostics, night vision, and chemical detection, all of which require detectors with high responsivity and low noise. APDs are particularly valuable in these areas due to their internal gain mechanism, which amplifies weak optical signals via carrier multiplication, enabling the detection of low-light and even single photons.[5]

Today, APDs based on III-V compound semiconductors, especially those based on InGaAs with InP or InAlAs multiplication layers, dominate the SWIR market up to ≈1700 nm. These APDs offer excellent performance metrics, with demonstrated data transmission rates up to 106 Gbit s^{-1}.[6] For longer wavelengths in the extended SWIR and mid-infrared other material systems such as AlInAsSb, InAs or HgCdTe are used.[7–9] However, these typically require cryogenic cooling to suppress dark current and noise, limiting their use in mobile or ambient-temperature environments. Moreover, III-V or II-VI compound semiconductors face noticeable limitations: they are expensive, and they rely on substrates that are smaller and incompatible with mainstream Si complementary metal-oxide-semiconductor (CMOS) technology.

To address these limitations, recent research has turned to group IV materials, such as Ge and GeSn. Ge-on-Si APDs were first demonstrated in 2007 and are now available in several Si photonics foundries, leveraging silicon's existing CMOS fabrication ecosystem.[10,11] These materials offer excellent compatibility with CMOS fabrication processes, providing a path toward monolithic integration of SWIR photodetectors on Si: a critical advancement for scalable, low-cost SWIR technology. This progress was recently highlighted by the demonstration of CMOS-compatible 10-pixel linear arrays of Ge-on-Si APDs.[12] GeSn alloys, formed by incorporating Sn into Ge, offer a tunable direct bandgap that extends the absorption edge of pure Ge from

M. Wanitzek, H. Ramachandra, C. Spieth, A. Daus, M. Oehme
Institute of Semiconductor Engineering
University of Stuttgart
Pfaffenwaldring 47, 70569 Stuttgart, Germany
E-mail: alwin.daus@iht.uni-stuttgart.de

J. Schulze
Chair of Electron Devices
Friedrich-Alexander-University Erlangen-Nürnberg
Schottkystraße 6, 91058 Erlangen, Germany

The ORCID identification number(s) for the author(s) of this article can be found under https://doi.org/10.1002/aelm.202500495

DOI: 10.1002/aelm.202500495

1.55 μm up to 4 μm at 15% Sn and beyond, depending on the Sn concentration.[13] This tunability enables GeSn-on-Si APDs to operate at a broad range of wavelengths.

In SWIR APDs, the separate absorption, charge, and multiplication (SACM) architecture is commonly employed to leverage the advantageous properties of different materials. For GeSn-on-Si APDs, the absorption layer is composed of GeSn, while the multiplication layer is Si. Si, with its low ionization coefficient for holes relative to electrons, is an ideal material for achieving low-noise avalanche gain, outperforming III-V multiplication layers such as InP and InAlAs in this respect.[14] Despite this promise, achieving low dark current in GeSn APDs remains a significant challenge, particularly at higher Sn concentrations where epitaxial defects and thermally generated carriers can degrade performance. GeSn-on-Si APDs have been under investigation since 2015, following the pioneering demonstration by Dong et al., who realized a SACM-structured device incorporating 5% Sn.[15] Their results showed avalanche behavior and a responsivity of ≈1 A W^{-1} at 1630 nm, validating the feasibility of GeSn as an absorber for extended SWIR detection. However, these devices were constrained by relatively high dark current larger than 100 μA before breakdown, moderate multiplication gains of approximately 10, and no demonstrated high-frequency performance. These limitations were largely attributed to the missing electric field management within the SACM structure and the early-stage of GeSn epitaxy at the time, which resulted in high threading dislocation densities. Subsequent studies predominantly explored GeSn p-i-n photodiodes, a structure consisting of a p-type, intrinsic, and n-type region, to improve material quality, while advancements in APD performance remained relatively modest.[16] More recently, refined growth techniques and device architectures have begun to address these issues, but further improvements are necessary to approach the maturity of Ge-on-Si and III-V-based APDs.

In parallel, APDs are increasingly explored for single-photon detection applications. This capability has been demonstrated in both Ge-on-Si and InGaAs/InP APDs.[17,18] Low dark count rates and high detection efficiency are essential for single-photon applications. While Ge-on-Si single-photon avalanche diodes (SPADs) have exhibited single-photon detection capability at room-temperature, this has so far only been demonstrated at a wavelength of 1310 nm.[19] Similarly, InGaAs/InP SPADs are limited to around 1670 nm.[20] GeSn, with its tunable bandgap, is therefore uniquely positioned to extend single-photon detection further to longer wavelengths within the SWIR range while remaining compatible with the Si technology. This could open the path to a wide range of quantum applications at longer wavelengths that are inaccessible with existing SPAD technologies.[21]

In this work, GeSn-on-Si APDs are developed and investigated with the goal of combining high responsivity, low dark current, and compatibility with Si integration platforms. Building on previous insights into surface leakage and electric field distribution, a tailored fabrication process for double-mesa structures was used. The double-mesa design addresses the challenge of high peripheral electric field and the resulting high dark current, an issue we previously investigated in Ge-on-Si APDs and SPADs.[22,23] The absorber layers are realized through high-quality molecular beam epitaxy (MBE) of pseudomorphic GeSn absorber layers on so-called "Ge-virtual substrates" (VS) on Si, allowing for efficient absorption of 1550 nm and beyond. Through these improvements a record-high responsivity at 1550 nm of 14.7 A W^{-1} with a dark current below 1 μA at the onset of avalanche breakdown are achieved. Our results indicate a promising pathway for high-performance, Si-compatible APDs in SWIR applications and underscore the potential of GeSn-on-Si APDs in applications ranging from telecommunications to single-photon SWIR detection and pave the way for further advancements in CMOS-integrated optoelectronics.

2. Device Overview and Working Principle

The GeSn-on-Si APDs were realized via MBE followed by a standard clean-room fabrication procedure to form circular shaped mesa diodes (details in Experimental Section). The device structure is illustrated in **Figure 1**, which includes a schematic cross-section and a top-view scanning electron microscopy (SEM) image of the completed device.

The diameter of the device d_{diode} refers to the diameter of the second mesa. The first mesa is structured to be smaller by a distance of x_{etch}, which is 5 μm for the 80 μm diameter device, resulting in a 70 μm diameter of the first mesa. Electric field simulations revealed that x_{etch} can be reduced to 2.5 μm without influencing the peripheral electric field. The optical window has a diameter of 48 μm. **Figure 2a** presents a schematic band diagram of the GeSn-on-Si APDs under reverse bias, illustrating their working principle. Photons with an energy greater than the bandgap energy of GeSn are absorbed, generating electron-hole pairs. The photogenerated electrons drift into the Si multiplication layer, where they undergo impact ionization, leading to avalanche gain. The band diagram shown is an approximate representation based on simulations and does not precisely depict the band-offset energies at the GeSn heterojunction. The GeSn-on-Si APDs demonstrated here utilize a double-mesa structure, which effectively reduces the peripheral electric field at the mesa sidewalls, while maintaining a high electric field in the active area of the device.[22,23] This field management suppresses surface leakage and enables low dark current without degrading responsivity and is confirmed by electric field simulations, as shown in Figure 2b. Simulation details can be found in the Experimental Section.

3. Results and Discussion

Following growth and fabrication, high-resolution x-ray diffraction (HR-XRD) measurements are carried out on all samples to determine the Sn content, the strain and overall crystal quality. **Figure 3a** shows the measurement of the symmetrical (004) diffraction as a high-resolution rocking curve (RC). The left graphs show the measurements of all three samples in the angle range between 65° and 67.5°, showing three distinct peaks. These are the GeSn peak of the absorption layer, the p^+ Ge peak arising from the extrinsically doped contact layer, and the Ge-VS peak, whereby only the GeSn reflection differs depending on the Sn content.[24] On the right, the narrow and high Si(004) reflections of each sample are displayed, which arise from the Si substrate. Additionally, the lateral lattice constant is determined from a reciprocal space map measurement of the asymmetric $(\bar{2}\,\bar{2}\,4)$ diffraction, and the corresponding space map is illustrated in Figure 3b.

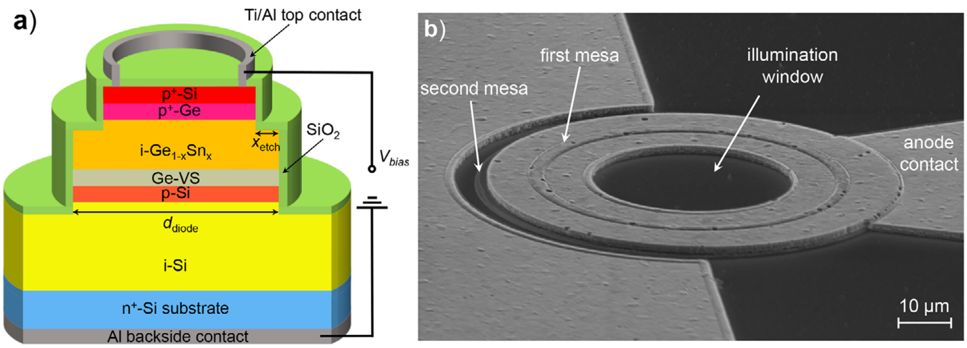

Figure 1. a) Schematic structure of the double-mesa GeSn-on-Si APDs and b) a top-view SEM image of a fabricated device with a diameter of 80 µm.

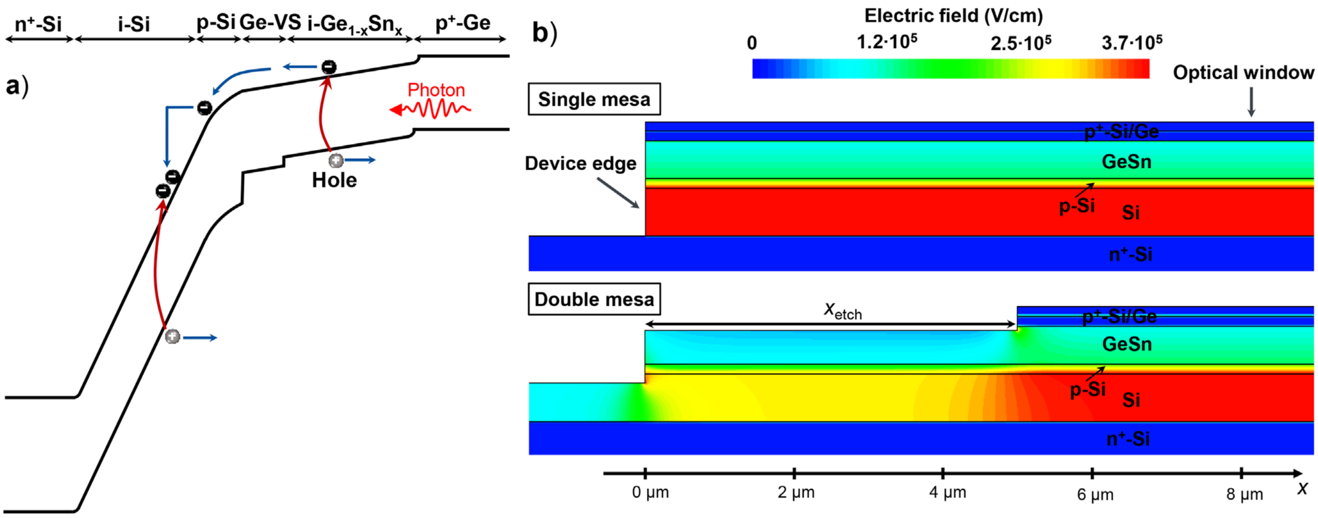

Figure 2. a) Schematic band diagram of the GeSn-on-Si APDs under reverse bias illustrating photon absorption and carrier multiplication. b) Simulated electric field distribution at the device edge, comparing the double-mesa structure to a conventional single mesa. The diameter of the device is 80 µm and the optical window and central active region extend toward the right-hand side, where the electric field remains high to allow for efficient charge transport and avalanche multiplication.

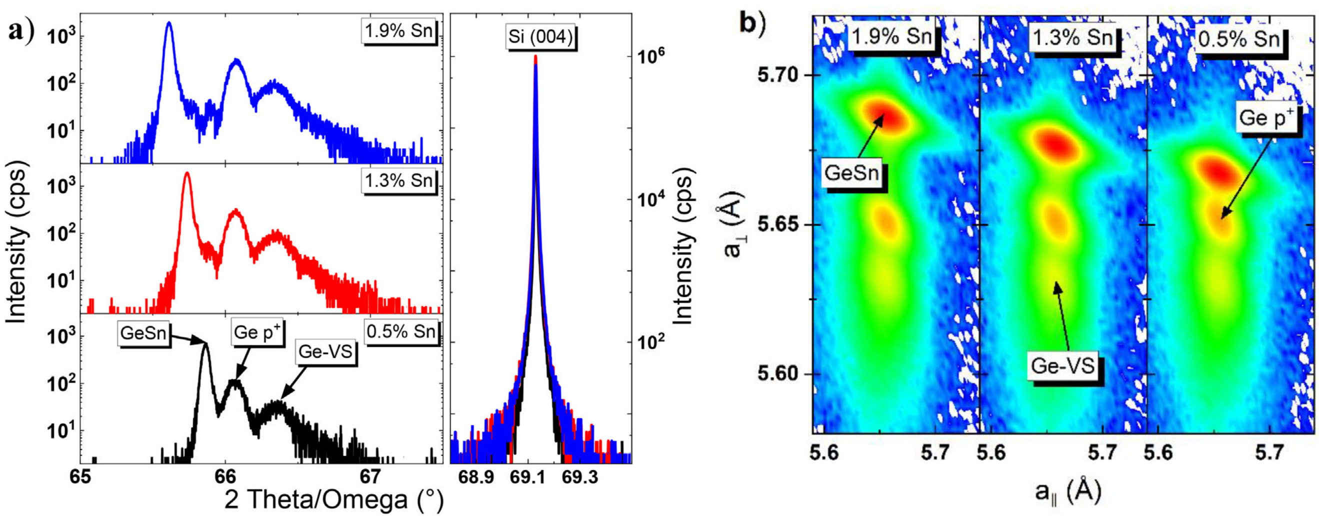

Figure 3. a) HR-XRD rocking curves of the symmetric (004) diffraction of the GeSn-on-Si APDs with various Sn concentration and b) the HR-XRD space maps of the asymmetric ($\bar{2}\bar{2}4$) diffraction of all samples. The GeSn absorption layer is pseudomorphically grown on the Ge-VS.

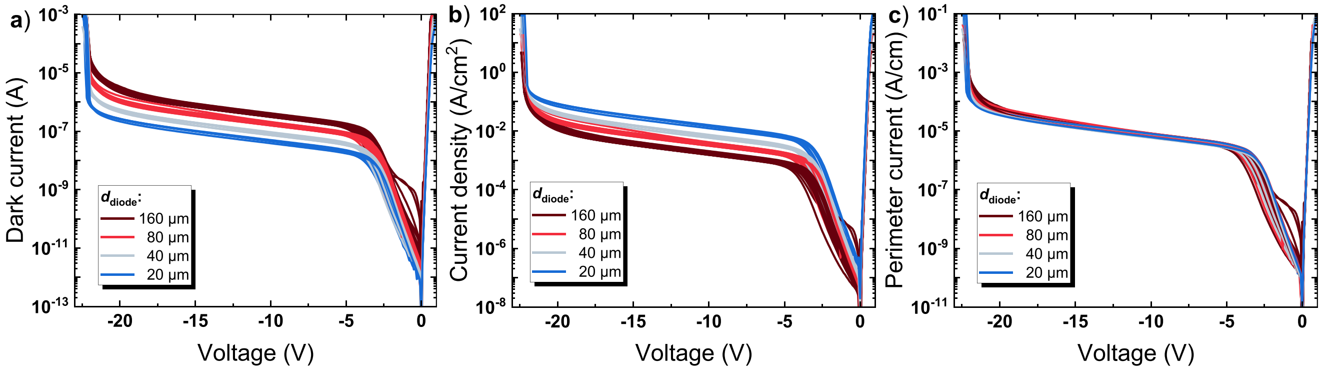

Figure 4. a) I_d of the double-mesa structure GeSn-on-Si APDs with 1.9% Sn for various diode diameters, b) I_d normalized to the area and c) I_d normalized to the perimeter of the devices indicating a leakage path on the perimeter of the diodes.

The space map shows the same three peaks. The p$^+$ Ge peak exhibits equal in-plane $a_{\|}$ and out-of-plane lattice parameters $a_{\perp}$, indicating that the layer is fully relaxed. In contrast, the GeSn peak shows a lateral lattice constant matching that of the underlying Ge-VS, confirming that it is pseudomorphic. By extracting the respective in-plane and out-of-plane lattice parameters for each individual peak, the unstrained lattice constant a_0 can be calculated by applying the linear elasticity theory:

$$\frac{a_{\perp}}{a_{\|}\,(vs)} = 1 + f\left(1 + \frac{2c_{12}}{c_{11}}\right) \quad (1)$$

This assumes biaxial deformation with the elastic constants c_{11} and c_{12} and the lattice mismatch f.[25] The reference grid for the pseudomorphic growth is the in-plane lattice spacing $a_{\|}(VS)$ of the virtual substrate. The biaxial strain ε is the negative of f, e.g. larger lattice constant $a_0(f > 0)$ provokes a compressive strain ($\varepsilon < 0$). With the help of Vegard's law, the Sn concentration can be determined for each sample.[26] The Sn content in the GeSn-on-Si APDs are 0.5%, 1.3%, and 1.9% respectively. The GeSn layers are pesudomorphic with a compressive strain, which increases for higher Sn concentrations. In the 0.5% Sn sample the strain is −0.13%, in the 1.3% it is −0.17%, and in the 1.9% Sn sample it is −0.29%. While the Sn leads to a reduction in the bandgap energy the compressive strain partly counteracts this and increases the bandgap energy compared to the unstrained state.

Figure 4a displays the dark current I_d of the APD with 1.9% Sn as a function of reverse bias voltage for devices of various diameters. The I_d increases with both reverse voltage and device diameter. Additionally, normalizing the I_d to the device area or perimeter reveals that the primary leakage current is perimeter-dependent, as observed in Figure 4b,c. This behavior contrasts typical GeSn-photodiodes, where I_d scales with device area due to bulk-dominated leakage.[27] The observed perimeter dependence indicates suppressed bulk leakage, made possible by high crystal quality and low defect density, pointing to the effectiveness of the epitaxial growth approach. This was observed in all samples regardless of the Sn concentration, as can be seen in the Figures S1 and S2, Supporting Information.

Figure 5a illustrates the dark current–voltage characteristics of the GeSn-on-Si APDs with varying Sn concentrations (0.5%, 1.3%, and 1.9%) for a fixed device diameter of $d_{diode} = 80$ µm. The results indicate no clear influence of Sn concentration on the I_d. Also, there is no influence of the Sn concentration on the breakdown voltage V_{BD} because V_{BD} is predominantly defined by the Si multiplication layer thickness. Nevertheless, V_{BD} varies slightly between −21.6 V for the 0.5% Sn and 1.3% Sn and −22.1 V for the 1.9% Sn samples, which is caused by minor thickness fluctuations of the Si multiplication layer. Temperature-dependent

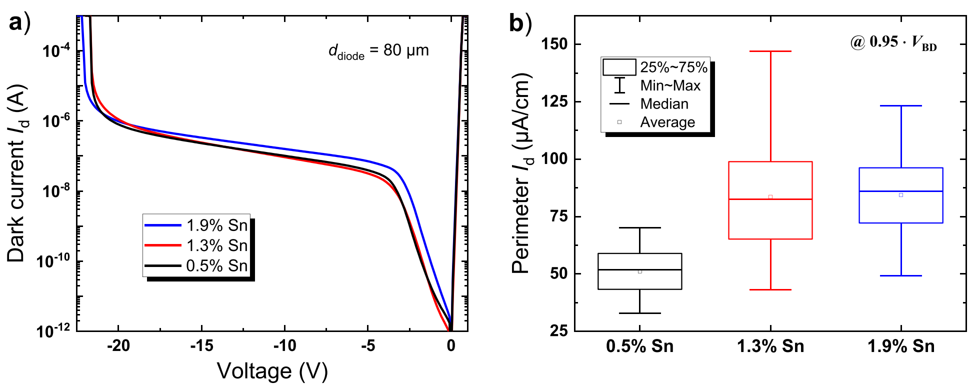

Figure 5. a) Comparison of the I_d-characteristics for different Sn concentrations and b) the box-plot of the perimeter I_d at 0.95 V_{DB}. The box plot consists of data of approximately 70 diodes for each sample.

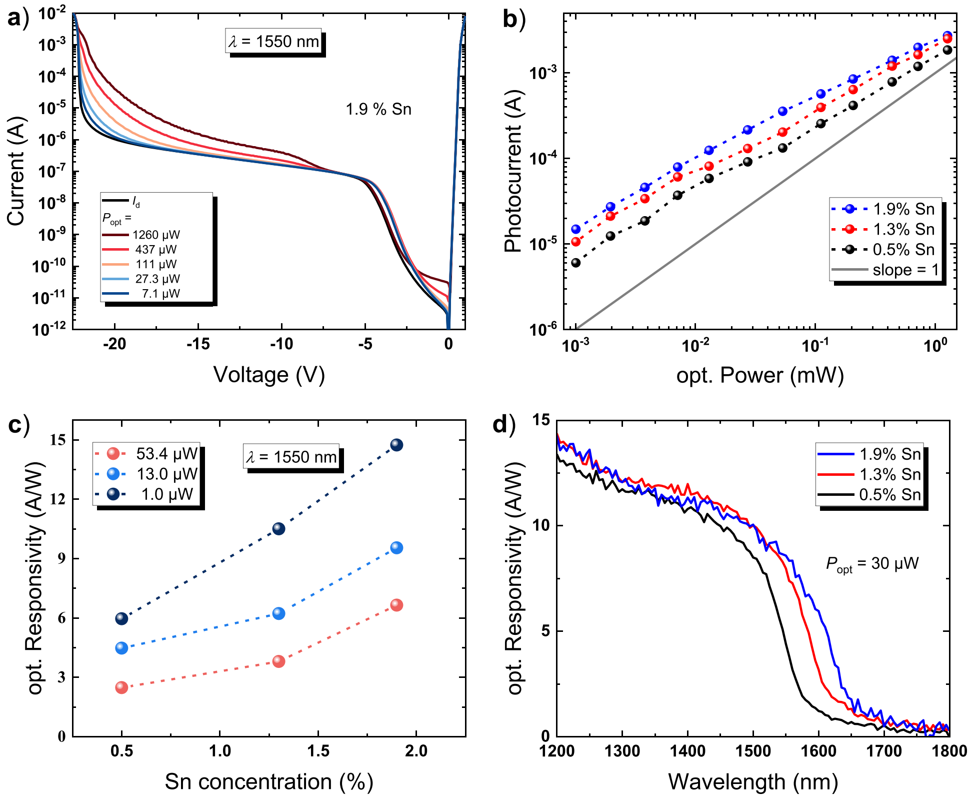

Figure 6. a) The current of the Ge-on-Si APD with 1.9% Sn under illumination of 1550 nm for P_{opt} ranging from 7.1 µW to 1.26 mW, and b) the calculated photocurrent as a function of the Sn concentration for various P_{opt}, and c) R_{opt} for three P_{opt} as a function of Sn concentration, and d) spectral R_{opt} measured at 30 µW using a ps-pulsed laser. Measurements were performed at a bias of −21.6 V for the 0.5% Sn and 1.3% Sn samples, and at −22.1 V for the 1.9% Sn sample.

analysis of the V_{BD} revealed a positive temperature coefficient of ≈0.013 V K^{-1}, confirming that the breakdown mechanism is indeed avalanche multiplication, see Figure S3, Supporting Information.

The devices were statistically analyzed for their I_d-characteristics using approximately 70 devices with four different device diameters (d_{diode} = 160, 80, 40, and 20 µm) across each sample. Figure 5b illustrates the box-plot of the perimeter current at a bias of 95% of V_{BD}, including the minimum, maximum, median, and mean values, along with the interquartile range (25%–75%) for each Sn concentration. The analysis shows that I_d is uniform across each sample, with the mean perimeter current increasing slightly from 50 to 87.5 µA cm^{-1} with higher Sn concentrations. This trend may result from the reduced bandgap of the GeSn alloy with increasing Sn content. Overall, the I_d in this work remains significantly lower than previously reported values. For example, the I_d at 95% of V_{BD} were reported as 85.9, 95.1, 2.73, and 30 mA cm^{-1} in earlier GeSn-on-Si APDs.[15,28–30] In comparison, the APDs with 1.9% Sn presented here achieve an average I_d of 84.37 µA cm^{-1}, which is a five-fold reduction relative to the previously reported lowest value of 450.8 µA cm^{-1}.[31] Figure S4, Supporting Information, illustrates the I_d-characteristics of this work in direct comparison with all previously reported GeSn-on-Si APDs. The significantly lower I_d achieved here suggests a pathway toward reduced dark count rates under Geiger-mode operation, which could make GeSn-on-Si APDs promising candidates for single-photon detection at 1550 nm. However, a systematic study of SPAD operation characteristics will be required to confirm this potential and will be the subject of future investigations.

Following the I_d analysis, measurements under illumination were carried out. **Figure 6a** depicts the current-voltage behavior of the GeSn-on-Si APD with 1.9% Sn under various incident optical power levels ranging from 7.1 to 1260 µW. A rise in current under illumination can be observed at around −8 V, which corresponds to the punch-through of the electric field into the GeSn absorption layer. At this voltage, the depletion region expands beyond the charge layer and begins to extend into the GeSn layer, enabling efficient separation and collection of photogenerated carriers. This transition also coincides with a local minimum in the device capacitance, as shown in of Figure S5, Supporting Information, reflecting the full depletion of the charge layer. However, the photocurrent at this voltage remains smaller than expected from a reference GeSn p-i-n diode, which is used to benchmark absorption efficiency. This discrepancy can be attributed to enhanced recombination in the GeSn layer or to residual energy barriers at the GeSn/Ge heterointerface that limit efficient carrier injection into the Si multiplication region. As the reverse bias increases further, these limitations are overcome, and the current rises strongly due to carrier multiplication, with unity gain achieved only at −20.8 V. The gain as a function of reverse voltage is provided in Figure S6, Supporting Information. The maximum photocurrent is generally observed at or slightly below the V_{BD}. This behavior is consistent across all three samples, as the overall shape of the photocurrent curve remains similar, although the absolute photocurrent decreases with lower Sn concentration. These measurements were performed identically for all samples, and the corresponding graphs are provided in Figure S7, Supporting Information.

Photocurrent measurements were also conducted for several more laser powers on all three samples. The results of these measurements are shown in Figure 6b–d, taken at a bias of −21.6 V for the 0.5% Sn and 1.3% Sn samples, and at −22.1 V for the 1.9% Sn sample. Figure 6b presents the measured photocurrent as a function of incident laser power. In the double logarithmic plot, the photocurrent follows a straight line with a slope different from one, indicating a nonlinear power-law relationship. This deviation arises from space-charge effects. At higher optical powers, the density of photogenerated carriers becomes large enough that their accumulated charge partially screens the internal electric field in the multiplication region. The reduced field not only slows carrier transport from the GeSn absorber into the Si multiplication layer but also lowers the impact ionization rate. As a result, the multiplication gain decreases with increasing optical power. This type of intensity-dependent responsivity has also been reported for Ge-on-Si and InGaAs APDs.[32,33] Figure 6c illustrates the optical responsivity R_{opt}, calculated by dividing the photocurrent by the laser power P_{opt}, as a function of the Sn concentration for three laser powers. A strong increase of the R_{opt} with increasing Sn concentration can be observed. At a laser power of 53.4 μW, the devices achieve R_{opt} values of 6.65, 3.80, and 2.48 A W^{-1} for Sn concentrations of 1.9%, 1.3% and 0.5%, respectively. The maximum R_{opt} are obtained at the lowest optical power of 1 μW, reaching 14.7 A W^{-1} (1.9% Sn), 10.5 A W^{-1} (1.3% Sn), and 6.0 A W^{-1} (0.5% Sn). These results represent a significant improvement over other recent works.[30] By dividing by the R_{opt} of a reference GeSn p-i-n diode ($R_{opt,PD} = 0.095$ A W^{-1}) with the same layer thickness, the multiplication gain can be calculated. This results in a gain of 154 for the 1.9% Sn sample.

Additionally, the spectral response of the GeSn-on-Si APDs was investigated and the results are illustrated in Figure 6d. The high responsivity at 1550 nm demonstrates the suitability of these APDs for fiber-optic communication systems. Moreover, an extended sensitivity at wavelengths beyond 1550 nm is observed with increasing Sn concentration. This performance improvement is attributed to the reduced bandgap of GeSn, which allows for efficient absorption of longer-wavelength photons. This redshift in absorption and R_{opt} for wavelengths above 1700 nm can be seen clearer in the logarithmic scaled graph in Figure S8, Supporting Information. Future work could explore higher Sn concentrations to extend the device's ability to the emerging 2 μm telecom band. As our epitaxial approach with the double-mesa device structure leads only to a small influence of the Sn content, these GeSn-on-Si APDs with higher Sn concentration could exhibit similar noise characteristics, underscoring their potential as high-performance detectors in emerging telecom applications. There is a slight discrepancy between the responsivities achieved using the ps-pulsed laser and the cw-laser. We attribute this to the high peak carrier density generated by the ps-pulses, which can lead to gain saturation due to the space-charge effects. Additionally, Auger recombination may contribute to carrier loss under these high-density conditions, further reducing the multiplication gain.

Lastly the bandwidth of the devices was characterized through impulse response measurement using the ps-pulsed laser and a sampling oscilloscope with a bandwidth of 16 GHz. **Figure 7a** displays the impulse response measurement of the GeSn-on-Si APD with 1.9% Sn at various bias voltages. As the reverse voltage increases, the amplitude of the response rises due to enhanced avalanche multiplication. Figure 7b presents the corresponding normalized frequency response extracted from the temporal signal. At reverse voltages below the V_{BD} of −22.1 V, a 3 dB bandwidth of 300 MHz is achieved for a device with $d_{diode} = 80$ μm. This relatively low value is caused by the large parasitic capacitance of approximately 8 pF, originating from the large metal pads. In contrast, the theoretical junction capacitance of the APD is estimated to be only ≈0.6 pF, which corresponds to a 3 dB bandwidth of 5.3 GHz when limited by the resistive-capacitive (RC) time constant. Optimization, such as reducing contact pad size or employing a localized buried n^{+} layer, would therefore significantly increase bandwidth. Further improvement toward bandwidths ≈60 GHz is possible through device down-scaling to ≈15 μm diameter. Interestingly, for reverse voltages exceeding the $|V_{BD}|$, an increase in bandwidth can be observed while maintaining consistent signal amplitude. This behavior is caused by resonance due to inductive peaking, a phenomenon well-documented in other APDs.[32] We recently reported that this also occurs in GeSn-on-Si APDs.[34] Therefore a 3-dB-bandwidth of 1.2 GHz is achieved at a voltage of −22.9 V. Further exploitation of the demonstrated inductive peaking can be achieved if the impedance of the APD is carefully designed, as has been demonstrated by Shi et al. achieving a 53 GHz bandwidth in Ge-on-Si APDs.[14]

In the literature a common figure of merit for comparing APDs is the gain-bandwidth-product (GBP), which evaluates their suitability for telecommunications applications. While the GBP successfully captures the trade-off between high gain and high bandwidths, it is only valid when comparing APDs made from the same material system. Because the gain is independent of absorption, the GBP does not fully account for the ability of the APD to detect specific optical signals. Therefore, we propose using the responsivity-bandwidth-product (RBP), which incorporates the signal strength by accounting for gain and quantum efficiency. Although less commonly used in the literature, the RBP offers greater insight into detection performance and allows for comparison across material systems.[35] For the demonstrated GeSn-on-Si APD, the achieved RBP is 17.6 A W^{-1} GHz^{-1} at 1550 nm, which corresponds to a GBP of 185 GHz when considering the reference responsivity of 0.095 A W^{-1}.

A comparative analysis of the R_{opt} at 1550 nm versus the corresponding I_d at that bias is presented in **Figure 8** for the GeSn-on-Si APDs from this study, alongside four previously reported devices, to highlight the advancements achieved in this work.[15,28,29,36] The APDs fabricated in this work exhibit superior performance, achieving an R_{opt} of 14.7 A W^{-1}, which significantly exceeds the previously reported maximum of 4.88 A W^{-1} at a wavelength of 1550 nm. In terms of I_d, our APDs exhibit notably lower values under most operating conditions compared to earlier studies. However, at bias voltages approaching the V_{BD}, where the gain and R_{opt} reach their maximum values, the I_d

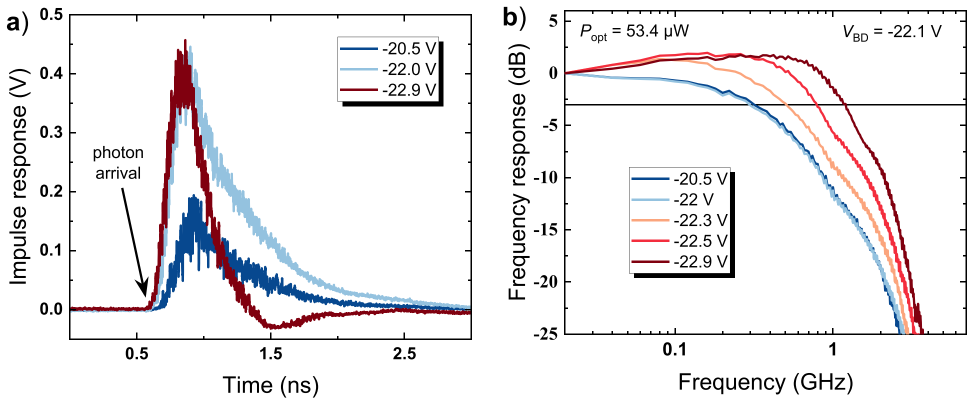

Figure 7. a) Impulse response at different bias voltages while illuminated by 53.4 µW at 1550 nm and b) normalized frequency response of an 80 µm diameter GeSn-on-Si APD with 1.9% Sn, showing an increased bandwidth at higher reverse voltages.

increases substantially. As a result, the I_d values under these conditions become comparable with those reported in other works from the literature. For consistent comparison, all dark current values are normalized to the device area, following common practice in the literature. While the dark current in our devices exhibits a clear perimeter dependence, we adopt area normalization to ensure compatibility with previously published values. This approach allows for direct benchmarking against prior work, even though it may underestimate the relative improvement achieved through our double-mesa design. Device diameters reported in the literature are 30 µm for ref.[15], 60 µm for refs.[28,29], and 160 µm for ref.[36]. The here presented performance improvements highlight the effectiveness of our fabrication process and material optimization strategies, such as the high-quality epitaxy on the Ge-VS, employed in this study. This demonstrates the potential of GeSn-on-Si APDs for high-sensitivity applications in the short-wave infrared spectral range.

In addition to R_{opt} and I_d, **Table 1** also highlights bandwidth-related performance. Our devices achieve a 3 dB bandwidth of 1.2 GHz with an 80 µm diameter, corresponding to a responsivity–bandwidth product of 17.6 A W^{-1} GHz^{-1}. While this is below the values reported for the most advanced Ge-on-Si and InGaAs/InP APDs, it represents a new benchmark for GeSn-on-Si devices. As discussed previously, bandwidths in the tens of GHz range should be achievable in GeSn-on-Si APDs through targeted device scaling and layout optimization.

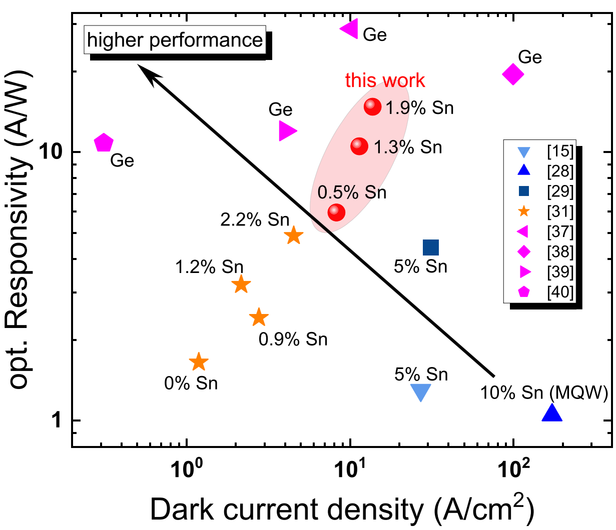

Figure 8. Comparison of the R_{opt} at 1550 nm versus the I_d for various GeSn-on-Si and Ge-on-Si APDs reported in the literature.

Additionally, the highest-performing Ge-on-Si APDs reported in the literature were included to contextualize our results with respect to state-of-the-art APDs.[37–40] The data show that Ge-on-Si APDs achieve up to twice the R_{opt} while maintaining similar dark current densities compared to our GeSn-on-Si APDs. This performance advantage is primarily due to their use of significantly thicker absorption layers (typically >1 µm) and the overall maturity of the Ge material platform compared to GeSn. Particularly in the longer wavelength range above 1550 nm, where conventional Ge-on-Si APDs exhibit limited absorption our GeSn-on-Si APDs already demonstrate superior performance. These results highlight the strong potential of GeSn for extended SWIR detection and suggest that further improvements in epitaxy and device design could enable GeSn-on-Si APDs to surpass pure Ge devices in both responsivity and spectral range, making them highly promising for next-generation SWIR applications.

4. Conclusion and Outlook

In summary, we demonstrated high performance GeSn-on-Si APDs with Sn concentrations up to 1.9%. We attribute the improved performance of our devices compared to prior works to high-quality MBE growth of pseudomorphic GeSn absorber layers on Ge-VS on Si substrates combined with a tailored fabrication process for double-mesa structures. Our devices show a notably reduced dark current, and the APD with 1.9% Sn achieved a maximum responsivity of 14.7 A W^{-1} at 1550 nm which is three times larger than previously reported values. Spectral responsivity measurements revealed an enhanced absorption at wavelengths beyond 1550 nm with increasing Sn concentrations. Additionally, impulse response measurements demonstrated a 3-dB bandwidth of 1.2 GHz for devices with an 80 µm diameter resulting in a responsivity-bandwidth-product of 17.6 A W^{-1} GHz^{-1}.

Table 1. Comparison of GeSn-on-Si APDs with Ge-on-Si and InGaAs/InP APDs operating at 1550 nm and room-temperature.

Material	Diameter [µm]	Breakdown voltage [V]	Responsivity [A W^{-1}]		Dark current [A]		3 dB Bandwidth [GHz]	Responsivity-bandwidth-product [A W^{-1} GHz]
			Unity gain	Maximum	Unity gain	Maximum		
This work	80	21.1	0.095	14.7	$1.5 \bullet 10^{-6}$	$43 \bullet 10^{-6}$	1.2	17.6
GeSn-on-Si[29]	60	14.5	0.15	4.4	$5.3 \bullet 10^{-6}$	$884 \bullet 10^{-6}$	1.0	4.4
GeSn-on-Si[15]	30	9.8	0.16	1.3	$1.6 \bullet 10^{-5}$	$9.8 \bullet 10^{-4}$	—	—
GeSn-on-Si[31]	80	21.7	0.11	0.4	$1.9 \bullet 10^{-6}$	$1.7 \bullet 10^{-5}$	—	—
Ge-on-Si[38]	10	26.5	0.35	19.5	$20 \bullet 10^{-9}$	$78 \bullet 10^{-6}$	12	234
Ge-on-Si[37]	50	55	0.41	28.8	$200 \bullet 10^{-9}$	$200 \bullet 10^{-6}$	—	—
InGaAs/InP[41]	35	33	0.94	36.7	$0.14 \bullet 10^{-9}$	$28 \bullet 10^{-9}$	8.3	304

While these results establish a new performance benchmark for GeSn-on-Si APDs, several opportunities for further advancement remain. The current bandwidth is limited by parasitic capacitance from the large contact pads. By optimizing device geometry and contact layout, the intrinsic junction capacitance could enable multi-GHz bandwidths, and device miniaturization down to ≈15 µm diameter or waveguide-coupled designs could push operation into the tens of GHz regime.[14] For imaging applications, scaling the circular mesa devices into pixel arrays is feasible, though careful optimization of the double-mesa geometry will be required to preserve fill factor. Beyond linear operation, the demonstrated devices are also promising candidates for single-photon detection. With proper operation in Geiger mode, the achieved low dark current could enable GeSn-on-Si SPADs that extend single-photon sensitivity beyond the wavelength range accessible with existing Ge-on-Si and InGaAs/InP devices.[42] Finally, increasing Sn concentration in the absorber provides a clear pathway to extend detection into the 2 µm telecom band and beyond.[43] While our current approach using pseudomorphic growth offers superior crystal quality, it is constrained by a critical thickness that limits absorber thickness at high Sn contents.[44] Strain-relaxed GeSn buffer layers, already employed in high-performance GeSn lasers, represent a promising alternative for realizing thicker absorbers at 10–12% Sn.[45] Overcoming the associated defect-related leakage will be key to enabling GeSn-on-Si APDs for mid-infrared detection and integrated optoelectronic platforms.

5. Experimental Section

Molecular Beam Epitaxy: The epitaxial sample structure was grown using molecular beam epitaxy (MBE).[46] The growth process started on n$^+$-Si (100) substrates with a doping concentration of $2 \bullet 10^{19}$ cm^{-3}, which act as the cathode contact. Before the MBE, the Si substrates underwent a thorough cleaning protocol involving sequential treatments with piranha solution, RCA 1 and 2, and HF solutions to ensure a contamination-free surface. The first layer deposited was a 500 nm thick (intrinsic) i-Si, serving as the multiplication layer. Hall measurements on test structures confirmed that the background doping is n-type with a concentration of approximately $1 \bullet 10^{14}$ cm^{-3}. Following this, a 100 nm thick charge layer was added, featuring a nominal p-type doping of $1.4 \bullet 10^{17}$ cm^{-3} to sustain a low electric field within the GeSn while ensuring effective impact ionization in the i-Si layer. To grow low-defect GeSn absorber layers, a lattice-matched Ge-virtual substrate (Ge-VS) on Si using a two-step epitaxial growth process was first created. A Ge-VS is a relaxed Ge buffer layer deposited on a Si wafer to accommodate the lattice mismatch between Si and Ge-based materials. This intermediate layer reduces strain and suppresses defect propagation into subsequent epitaxial layers. This process involves the low-temperature growth of a 100 nm thick Ge seed layer, followed by high-temperature annealing at approximately 820 °C. In previous studies, it is demonstrated that this approach results in low-dark current Ge p-i-n diodes and yields threading dislocation densities on the order of $1 \bullet 10^7$ cm^{-2}.[47] Subsequently, a 300 nm thick intrinsic GeSn absorption layer was grown on the Ge-VS at a substrate temperature of 160 °C. Using this approach, the GeSn grows pseudomorphically without generating additional threading dislocations. Both the Ge and GeSn have a p-type background doping with a doping concentration of $5 \bullet 10^{15}$ cm^{-3} in the Ge and $1 \bullet 10^{16}$ cm^{-3} in the GeSn.[48] The Sn concentration of the GeSn layer was varied in three different samples to later analyze the influence of the Sn on device performance. Both the i-Si and the GeSn were specifically designed to be thin to achieve a low breakdown voltage, easing integration goals. The anode contacts of the GeSn-on-Si APDs consist of a 211 nm thick Ge/Si p+ hetero layer, doped at $1 \bullet 10^{20}$ cm^{-3}. This structure was chosen to provide effective surface passivation and ease of fabrication.

X-Ray Diffraction: High-resolution X-ray diffraction (HR-XRD) was performed on all fabricated samples to assess the structural properties of the epitaxial layers. A Rigaku Smartlab system equipped with a Cu Kα1 source (λ = 1.5406 Å) was used. The symmetrical (004) diffraction was measured using a 0D detector, and the asymmetric ($\bar{2}\ \bar{2}\ 4$) diffraction using a 1D detector.

Device Fabrication: The fabrication of the devices followed standard cleanroom procedures, starting with mesa formation through inductively coupled plasma reactive ion etching (ICP-RIE) using HBr as the etching gas. The process used 600 W coil power with 120 W platen power at a chamber pressure of 2.5 mTorr. The first mesa has an etch depth of approximately 250 nm, as it is necessary to etch through the Ge/Si p+ layer to ensure proper device functionality. The second mesa was etched an additional 500 nm to safely stop inside the Si multiplication layer. The samples were cleaned in ultrasonic baths of acetone and isopropanol, followed by a rinse in deionized water. Native oxide layers were removed using a sequential dip in 2.5% HF and 13% HCl solutions. The SiO_2 passivation layer was deposited using a plasma-enhanced chemical vapor deposition using tetraethyl orthosilicate and O_2 as the precursors at a temperature of 390 °C. The process parameters were 20 W of plasma power at a chamber pressure of 265 mTorr. The contact pads were structured through reactive ion etching with CHF_3 gas at a chamber pressure of 38 mTorr and 150 W plasma power. The metal contacts were deposited using Ar-sputtering and consist of a Ti/Al-stack (50 nm/1200 nm). The Ti interlayer prevents Al spiking. The metal contacts were again structured using ICP-RIE with HBr.

Simulation: Electric field simulations and schematic energy band diagrams were generated using the Sentaurus TCAD suite from Synopsys. The simulated layer structure corresponds exactly to the experimental device stack described in the epitaxy section, including the GeSn absorption layer, intrinsic Ge spacer, charge layer, and Si multiplication region. A fine mesh of 10 nm by 10 nm was implemented. The simulations were used to investigate the vertical electric field distribution across the APD. The simulations guided the development of the double-mesa design by helping to assess lateral field spreading near the mesa edge.

Electro-Optical Characterization: The electro-optical characterization of all samples is carried out using an on-wafer measurement system at a controlled temperature of 293 K. The devices are contacted using probe needles and measured through a Keithley 2636B source-measure unit. By employing low-leakage triaxial cables, the overall noise floor of the measurement setup was reduced to below 1 pA. For the illumination a continuous-wave (cw) laser at 1550 nm was vertically coupled onto the devices via a single-mode fiber. The laser power was calibrated using an InGaAs photodiode. Overall the current–voltage measurements show great accuracy and reproducibility. Even at high reverse voltage, where the dark current is elevated and the maximum R_{opt} values are achieved, the current measurement accuracy is ≈40 nA, while the minimum measured photocurrent is in the range of 14 μA. Additionally, the spectral response of the GeSn-on-Si APDs was investigated using a picosecond(ps)-pulsed supercontinuum white-light laser (NKT SuperK Extreme EXR-15) equipped with an acousto-optic tunable filter. The measurements were performed between 1200 nm and 1800 nm in wavelength steps of 5 nm. Prior to the measurements the laser power was calibrated to deliver a constant power of 30 μW for all wavelengths as otherwise the gain of the APD would be wavelength dependent. The impulse response measurements were performed using the same ps-pulsed laser at 1550 nm. The devices were mounted on a custom high-frequency printed-circuit board out of Polytetrafluoroethylene and connected to a SMA connector. The devices were then connected to a direct-current (dc) source and a sampling oscilloscope (PicoScope 9404-16) with a bandwidth of 16 GHz through a bias tee (Anritsu K251).

Supporting Information

Supporting Information is available from the Wiley Online Library or from the author.

Acknowledgements

The research leading to these results was part of the AI-SEE project, which is a co-labeled PENTA and EURIPIDES^2 project endorsed by EUREKA (grant number: 16ME0346). Co-funding is provided by the following National Funding Authorities: Austrian Research Promotion Agency (FFG), Business Finland, Federal Ministry of Education and Research (BMBF) and National Research Council of Canada Industrial Research Assistance Program (NRC-IRAP). Additional funding was provided by the Deutsche Forschungsgemeinschaft (DFG, German Research Foundation) - 431314977/GRK2642.

Conflict of Interest

The authors declare no conflict of interest.

Data Availability Statement

The data that support the findings of this study are openly available at Zenodo, reference https://doi.org/10.5281/zenodo.15746540.

Keywords

avalanche photodiodes, dark current, GeSn, molecular beam epitaxy, responsivity, short-wave infrared, telecommunications

Received: July 23, 2025
Revised: October 29, 2025
Published online: December 4, 2025

[1] M. P. Hansen, D. S. Malchow, *Proc. SPIE* **2008**, *6939*, 69390I, https://doi.org/10.1117/12.777776.
[2] J. C. Campbell, *J. Lightwave Technol.* **2007**, *25*, 109. https://doi.org/10.1109/JLT.2006.888481.
[3] M. A. Itzler, M. Entwistle, U. Krishnamachari, M. Owens, X. Jiang, K. Slomkowski, S. Rangwala, *Proc. SPIE* **2014**, *9114*, 91140F. https://doi.org/10.1117/12.2050798.
[4] R. G. Driggers, V. Hodgkin, R. Vollmerhausen, *Proc. SPIE* **2013**, *8706*, 87060L https://doi.org/10.1117/12.2016467.
[5] Y. Miao, H. Lin, B. Li, T. Dong, C. He, J. Du, X. Zhao, Z. Zhou, J. Su, H. Wang, Y. Dong, B. Lu, L. Dong, H. H. Radamson, *Nanomaterials* **2023**, *13*, 606. https://doi.org/10.3390/nano13030606.
[6] M. Nada, T. Yoshimatsu, F. Nakajima, K. Sano, H. Matsuzaki, *J. Lightwave Technol.* **2019**, *37*, 260. https://doi.org/10.1109/JLT.2018.2871508.
[7] H. Jung, S. Lee, X. Jin, Y. Liu, T. J. Ronningen, C. H. Grein, J. P. R. David, S. Krishna, *Commun. Mater.* **2024**, *5*, 219. https://doi.org/10.1038/s43246-024-00627-9.
[8] P. J. Ker, J. P. R. David, C. H. Tan, *Opt. Express* **2012**, *20*, 29568. https://doi.org/10.1364/OE.20.029568.
[9] P. D. Anderson, J. D. Beck, W. Sullivan, C. Schaake, J. McCurdy, M. Skokan, P. Mitra, X. Sun, *J. Electron. Mater.* **2022**, *51*, 6803. https://doi.org/10.1007/s11664-022-09873-4.
[10] Y. Kang, H.-D. Liu, M. Morse, M. J. Paniccia, M. Zadka, S. Litski, G. Sarid, A. Pauchard, Y.-H. Kuo, H.-W. Chen, W. S. Zaoui, J. E. Bowers, A. Beling, D. C. McIntosh, X. Zheng, J. C. Campbell, *Nat. Photonics* **2009**, *3*, 59. https://doi.org/10.1038/nphoton.2008.247.
[11] R. Soref, *IEEE J. Sel. Top. Quantum Electron.* **2006**, *12*, 1678. https://doi.org/10.1109/JSTQE.2006.883151.
[12] M. Modak, M. M. A. Mirza, X. Yi, Q. Tian, L. Saalbach, F. Fleming, J. Kirdoda, D. C. S. Dumas, X. Jin, C. Smith, L. Tegg, S. A. Yamini, J. P. R. David, D. J. Paul, R. W. Millar, G. S. Buller, *Adv. Photonics Res.* **2025**, *6*, 2500005. https://doi.org/10.1002/adpr.202500005.
[13] G.-E. Chang, S.-Q. Yu, G. Sun, *Sensors* **2023**, *23*, 7386. https://doi.org/10.3390/s23177386.
[14] Y. Shi, X. Li, G. Chen, M. Zou, H. Cai, Y. Yu, X. Zhang, *Nat. Photonics* **2024**, *18*, 610. https://doi.org/10.1038/s41566-024-01421-2.
[15] Y. Dong, G. Liang, Y.-C. Yeo, W. Wang, X. Xu, X. Gong, D. Lei, Q. Zhou, Z. Xu, W. K. Loke, S.-F. Yoon, *IEEE Trans. Electron Devices* **2015**, *62*, 128. https://doi.org/10.1109/TED.2014.2366205.
[16] V. Reboud, O. Concepción, W. Du, M. El Kurdi, J. M. Hartmann, Z. Ikonic, S. Assali, N. Pauc, V. Calvo, C. Cardoux, E. Kroemer, N. Coudurier, P. Rodriguez, S.-Q. Yu, D. Buca, A. Chelnokov, *Photonics Nanostruct.: Fundam. Appl.* **2024**, *58*, 101233. https://doi.org/10.1016/j.photonics.2024.101233.
[17] P. Vines, K. Kuzmenko, J. Kirdoda, D. C. S. Dumas, M. M. Mirza, R. W. Millar, D. J. Paul, G. S. Buller, *Nat. Commun.* **2019**, *10*, 1086. https://doi.org/10.1038/s41467-019-08830-w.
[18] A. Tosi, N. Calandri, M. Sanzaro, F. Acerbi Low-Noise, *IEEE J. Sel. Top. Quantum Electron.* **2014**, *20*, 192. https://doi.org/10.1109/JSTQE.2014.2328440.
[19] N. Na, Y.-C. Lu, Y.-H. Liu, P.-W. Chen, Y.-C. Lai, Y.-R. Lin, C.-C. Lin, T. Shia, C.-H. Cheng, S.-L. Chen, *Nature* **2024**, *627*, 295. https://doi.org/10.1038/s41586-024-07076-x.
[20] J. Zhang, M. A. Itzler, H. Zbinden, J.-W. Pan, *Light: Sci. Appl.* **2015**, *4*, 286. https://doi.org/10.1038/lsa.2015.59.
[21] S. Dello Russo, A. Elefante, D. Dequal, D. K. Pallotti, L. Santamaria Amato, F. Sgobba, M. Siciliani de Cumis, *Photonics* **2022**, *9*, 470. https://doi.org/10.3390/photonics9070470.
[22] M. Wanitzek, M. Hack, H. Ramachandra, L. Seidel, D. Schwarz, J. Schulze, M. Oehme, *Proc. SPIE* **2024**, *13109*, 1310907. https://doi.org/10.1117/12.3028061.
[23] M. Wanitzek, J. Schulze, M. Oehme, *Opt. Lett.* **2024**, *49*, 6345. https://doi.org/10.1364/OL.534436.

[24] M. Oehme, D. Widmann, K. Kostecki, P. Zaumseil, B. Schwartz, M. Gollhofer, R. Koerner, S. Bechler, M. Kittler, E. Kasper, J. Schulze, *Opt. Lett.* **2014**, *39*, 4711. https://doi.org/10.1364/OL.39.004711.
[25] J. Kouvetakis, J. Menendez, A. Chizmeshya, *Annu. Rev. Mater. Res.* **2006**, *36*, 497. https://doi.org/10.1146/annurev.matsci.36.090804.095159.
[26] L. Vegard, *Z. Phys.* **1921**, *5*, 17. https://doi.org/10.1007/BF01349680.
[27] M. Oehme, M. Wanitzek, C. Spieth, L. Seidel, M. Hack, E. Kasper, D. Schwarz, *J. Vac. Sci. Technol. B* **2024**, *42*, 033202. https://doi.org/10.1116/6.0003556.
[28] Y. Dong, W. Wang, S. Y. Lee, D. Lei, X. Gong, W. K. Loke, S.-F. Yoon, G. Liang, Y.-C. Yeo, *Semicond. Sci. Technol.* **2016**, *31*, 095001. https://doi.org/10.1088/0268-1242/31/9/095001.
[29] D. Zhang, X. Hu, D. Liu, X. Lin, W. Wang, Z. Ding, Z. Wang, B. Cheng, C. Xue, *Proc. SPIE* **2018**, *10846*, 108461B. https://doi.org/10.1117/12.2504669.
[30] J. Rudie, S. Amoah, X. Wang, R. Kumar, G. Abernathy, S. Akwabli, P. C. Grant, J. Liu, B. Li, W. Du, S.-Q. Yu, *IEEE J. Sel. Top. Quantum Electron.* **2025**, *31*, 3800708. https://doi.org/10.1109/JSTQE.2024.3482257.
[31] M. Wanitzek, M. Hack, D. Schwarz, J. Schulze, M. Oehme, *Mater. Sci. Semicond. Process.* **2024**, *176*, 108303. https://doi.org/10.1016/j.mssp.2024.108303.
[32] W. S. Zaoui, H.-W. Chen, J. E. Bowers, Y. Kang, M. Morse, M. J. Paniccia, A. Pauchard, J. C. Campbell, *Opt. Express* **2009**, *17*, 12641. https://doi.org/10.1364/oe.17.012641.
[33] J. W. Parks, A. W. Smith, K. F. Brennan, L. E. Tarof, *IEEE Trans. Electron Devices* **1996**, *43*, 2113. https://doi.org/10.1109/16.544382.
[34] M. Wanitzek, D. Schwarz, J. Schulze, M. Oehme, in *2024 IEEE Silicon Photonics Conf. (SiPhotonics)*, IEEE, Piscataway, NJ **2024**, pp. 1–2. https://doi.org/10.1109/SiPhotonics60897.2024.10543351.
[35] M. Nada, Y. Muramoto, H. Yokoyama, T. Ishibashi, S. Kodama, *Electron. Lett.* **2012**, *48*, 397. https://doi.org/10.1049/el.2012.0100.
[36] M. Wanitzek, M. Oehme, C. Spieth, D. Schwarz, L. Seidel, J. Schulze, in *ESSCIRC 2022- IEEE 48th European Solid State Circuits Conf (ESSCIRC)*, IEEE, Piscataway, NJ **2022**, pp. 169–172. https://doi.org/10.1109/ESSCIRC55480.2022.9911363.
[37] F. Fleming, X. Yi, M. M. A. Mirza, X. Jin, J. Kirdoda, D. C. S. Dumas, L. Saalbach, M. Modak, D. A. S. Muir, C. Smith, C. Coughlan, Q. Tian, R. W. Millar, J. P. R. David, D. J. Paul, G. S. Buller, *Opt. Express* **2024**, *32*, 19449. https://doi.org/10.1364/OE.521417.
[38] G. Kim, S. Kim, S. A. Kim, J. H. Oh, K.-S. Jang, *Opt. Lett.* **2018**, *43*, 5583. https://doi.org/10.1364/OL.43.005583.
[39] N. Duan, T.-Y. Liow, A. E.-J. Lim, L. Ding, G. Q. Lo, *Opt. Express* **2012**, *20*, 11031. https://doi.org/10.1364/OE.20.011031.
[40] M. Huang, S. Li, P. Cai, G. Hou, T.-I. Su, W. Chen, C. Hong, D. Pan, *IEEE J. Sel. Top. Quantum Electron.* **2018**, *24*, 3800911. https://doi.org/10.1109/JSTQE.2017.2749958.
[41] A.-W. Yue, R.-F. Wang, B. Xiong, J. Shi, *Chin. Phys. Lett.* **2013**, *30*, 038501. https://doi.org/10.1088/0256-307X/30/3/038501.
[42] R. A. Soref, F. de Leonardis, V. M. N. Passaro, *ACS Appl. Nano Mater.* **2019**, *2*, 7503. https://doi.org/10.1021/acsanm.9b01453.
[43] J. Rudie, X. Wang, R. Kumar, G. Abernathy, S. Amoah, S. Akwabli, H. Stanchu, P. C. Grant, B. Li, W. Du, J. Liu, S.-Q. Yu, *APL Photonics* **2025**, *10*, 106110. https://doi.org/10.1063/5.0286160.
[44] M. Oehme, K. Kostecki, M. Schmid, F. Oliveira, E. Kasper, J. Schulze, *Thin Solid Films* **2014**, *557*, 169. https://doi.org/10.1016/j.tsf.2013.10.064.
[45] L. Seidel, T. Liu, O. Concepción, B. Marzban, V. Kiyek, D. Spirito, D. Schwarz, A. Benkhelifa, J. Schulze, Z. Ikonic, J.-M. Hartmann, A. Chelnokov, J. Witzens, G. Capellini, M. Oehme, D. Grützmacher, D. Buca, *Nat. Commun.* **2024**, *15*, 10502. https://doi.org/10.1038/s41467-024-54873-z.
[46] D. Schwarz, M. Oehme, E. Kasper, in *Thin Films - Growth, Characterization and Electrochemical Applications* (Eds: F. Sarf, E. Yakar, I. Karaduman Er), IntechOpen, London **2024**. https://doi.org/10.5772/intechopen.114058.
[47] M. Oehme, M. Kaschel, S. Epple, M. Wanitzek, Z. Yu, D. Schwarz, A.-C. Kollner, J. N. Burghartz, J. Schulze, *IEEE Sens. J.* **2021**, *21*, 18696. https://doi.org/10.1109/JSEN.2021.3091203.
[48] M. Oehme, K. Kostecki, K. Ye, S. Bechler, K. Ulbricht, M. Schmid, M. Kaschel, M. Gollhofer, R. Körner, W. Zhang, E. Kasper, J. Schulze, *Opt. Express* **2014**, *22*, 839. https://doi.org/10.1364/OE.22.000839.